NJC

Accepted Manuscript

This article can be cited before page numbers have been issued, to do this please use: C. Villa-Pérez, I. C. Ortega, A. Vélez-Macías, A. M. Payán, G. A. Echeverría, D. B. Soria and G. C. Valencia-Uribe, *New J. Chem.*, 2018, DOI: 10.1039/C8NJ00661J.

ROYAL SOCIETY OF CHEMISTRY

rsc.li/njc

View Article Online
DOI: 10.1039/C8NJ00661J

NJC

ARTICLE

Crystal Structure, Physicochemical Properties, Hirshfeld Surface Analysis and Antibacterial Activity Assays of Transition Metal Complexes of 6-Methoxyquinoline†

Received 00th January 20xx,
Accepted 00th January 20xx

DOI: 10.1039/x0xx00000x

www.rsc.org/

C. Villa-Pérez, [a] I. C. Ortega, [b] A. Vélez-Macías, [b] A. M. Payán, [b] G. A. Echeverría, [c] D. B. Soria *[a] and G. C. Valencia-Uribe *[b]

Five monomeric complexes of Co(II), Cu(II), Ni(II), Zn(II) and Ag(I) with 6-methoxyquinoline (6-MeOQ) as ligand have been prepared, and their crystal structures have been determined by single X-ray diffractions. The Cu(II), Ni(II) and Zn(II) complexes are formulated as $M(6\text{-MeOQ})_2Cl_2$, completing MN_2Cl_2 coordination spheres. On the other hand, Co(II) and Ag(I) compounds are ionic with formulae $[Ag(6\text{-MeOQ})_2]^+$ NO_3^- and $H(6\text{-MeOQ})^+[Co(6\text{-MeOQ})Cl_3]^-$ (where $H(6\text{-MeOQ})^+$ is the protonated ligand). Hirshfeld surface analysis was employed to study the intermolecular interactions in the crystal lattices and from these studies it was found that π-stacking contacts play an important role. Besides, the complexes have been characterized by FTIR, UV-Visible and emission spectroscopies. The singlet oxygen production and fluorescence quantum yields were measured for all the complexes employing steady-state methodologies. Finally, the antibacterial activity of the complexes was screened against both Gram-positive and Gram-negative bacteria.

1. Introduction

6-Metoxiquinoline (6-MeOQ) can be found in the chemical structure of several antimalarial drugs [1]. This compound has been extensively studied regarding its photochemical behavior, and noteworthy singlet oxygen and fluorescence quantum yields have been reported [2–6]. Therefore, complexation of 6-MeOQ with transition metals could improve its photophysical properties and enhance its stability. However, only some coordination compounds with this ligand have been reported [3,7,8]. The spectroscopic and thermogravimetric properties of Co(II), Cu(II) and Zn(II) complexes were previously discussed, but their crystal structures were not determined[7]. As part of our ongoing research, we have reported the crystal structure and the physicochemical characterization of a Hg(II) compound [3] and a Co(II) ternary complex [8] with 6-MeOQ as ligand. Magnetic susceptibility measurements for the Co(II) complex have shown that it displays relaxation of the magnetization below a temperature of 9 K behaving as a SIM (single ion magnet). In the case of the Hg(II) complex, it could be used in advanced oxidation processes due to its considerably high singlet oxygen generation yield. The complexation of quinoline derivatives with transition metals has led to the discovery of new compounds with interesting structural, photophysical and biological properties. The photophysical properties of some quinoline derivatives with transition metals have been explored and they have been proposed as candidates as fluorescent probes and light emitting devices [9–11]. Some metal complexes of quinoline Schiff bases [12–14] and thioether [15–17] derivatives have shown better bactericidal effect as compared with the free ligands against Gram-negative and Gram-positive bacteria. Due to the versatile properties of metal complexes with 6-MeOQ as ligand and to study their coordination properties we herein report the crystal structure of Co(II) (**I**), Ni(II) (**II**), Cu(II) (**III**), Zn(II) (**IV**) and Ag(I) (**V**) complexes. The supramolecular arrangements of these complexes have an important contribution of several intermolecular interactions that have been studied by using the Hirshfeld surface analysis. Besides, vibrational and electronic spectroscopies have been used to characterize only the compounds **II** and **V**. Additionally, thermogravimetric analyses were used to study

[a] CEQUINOR, Departamento de Química, Facultad de Ciencias Exactas, Universidad Nacional de la Plata, La Plata (Argentina). E-Mail: soria@quimica.unlp.edu.ar
[b] GIAFOT, Departamento de Química, Facultad de Ciencias, Universidad Nacional de Colombia - Sede Medellín, Medellín (Colombia). E-Mail: gcvalenc@unal.edu.co
[c] IFLP - LANADI, Departamento de Física, Facultad de Ciencias Exactas, Universidad Nacional de La Plata, La Plata (Argentina).
† Electronic Supplementary Information (ESI) available: CCDC 1814014 - 1814018. See DOI: 10.1039/x0xx00000x

View Article Online
DOI: 10.1039/C8NJ00661J

their thermal behavior. Fluorescence and singlet oxygen quantum yields were also measured for all the complexes and the free ligand. With the aim of expanding the physicochemical studies and include biological tests, bacterial susceptibility was screened in both Gram-Negative and Gram-Positive bacteria.

2. Experimental

2.1 Synthesis of the Complexes

*Synthesis of complexes **I, III** and **IV***

The complexes $[H(6\text{-MeOQ})^+$ $[CoCl_3(6\text{-MeOQ})]^-]$ (**I**) and $[MCl_2(6\text{-MeOQ})_2]$ (M=Cu(II) (**III**) and Zn(II) (**IV**)), were prepared following the procedure described by Allan, *et al* [7]. 1 mmol of 6-MeOQ was added to a warm ethanolic solution containing 0.5 mmol of the corresponding MCl_2 salt (M = Co(II), Cu(II) and Zn(II)). After stirring the reaction for 1 h, blue, olive green and white solids precipitated for **I**, **III** and **IV**, respectively. Then the solids were filtered, washed several times with ethanol and dried at 60 ºC in an oven. The filtered solutions were left to stand, and after a few days well-developed crystals were obtained and used in single crystal X-ray determinations. Yields: 81.7, 93.4 and 87.0 % for **I**, **III** and **IV**, respectively. The elemental analyses (EA [%]) gave the following results: **I** ($CoC_{20}H_{19}N_2O_2Cl_3$): Exp. (calc.): C: 49.26 (49.56); H: 4.01 (3.95); N: 5.73 (5.78) %; **III** ($CuC_{20}H_{18}N_2O_2Cl_2$): C: 53.38 (53.05); H: 4.07 (4.01); N: 6.25 (6.19) %; **IV** ($ZnC_{20}H_{18}N_2O_2Cl_2$): C: 52.38 (52.83); H: 4.07 (3.99); N: 6.12 (6.16) %.

*Synthesis of complex **II***

The compound $[NiCl_2(6\text{-MeOQ})_2]$ was synthesized under solvent-free conditions by manually grinding 1 mmol of 6-MeOQ with 0.5 mmol of $NiCl_2{\cdot}6H_2O$ in an agate mortar for 15 minutes. During that process, a green oil was obtained and then it was heated to 60 ºC for 12 h. The resulting blue powder was washed with n-hexane (5 x 2 ml). Yield: 69.6 %. To obtain suitable crystals for X-ray analysis another experimental procedure was followed by refluxing an ethanolic solution containing 6-MeOQ and $NiCl_2{\cdot}6H_2O$ (2:1) for 6 h. A yellow precipitate was discarded, and after a few days, blue crystals were separated from the mother liquor. The EA [%] gave the following results: **II** ($NiC_{20}H_{18}N_2O_2Cl_2$): C: 53.48 (53.62); H: 4.01 (4.05); N: 6.11 (6.25) %.

*Synthesis of complex **V***

The $[Ag(6\text{-MeOQ})_2]$ NO_3 complex was synthesized following the same procedure as **I**, **III** and **IV**, but using $AgNO_3$ instead of the MCl_2 salt. No apparent changes were observed in the solution during the reaction; however, X-ray suitable white crystals were produced overnight, then they were filtered and washed with ethanol and hot distilled water. The synthesis and the manipulation of this complex were performed avoiding the exposure to light. Yield: 86.5 %. MP: 167 ºC. The EA [%] gave the following results ($AgC_{20}H_{18}N_3O_5$): C: 49.18 (49.20); H: 3.68 (3.72); N: 8.49 (8.61) %.

2.2 Materials and Methods

All the reagents were obtained from commercial sources and used without further purification, 6-Methoxyquinoline was obtained from Alfa-Aesar, Rose Bengal (RB) and 9,10-dimethylanthracene (DMA) were obtained from Sigma-Aldrich and Tego 51 from Merck Millipore. The FTIR spectra were carried out with a Bruker Equinox 55 spectrophotometer, in the range from 4000 to 400 cm^{-1} by using the KBr pellet technique with a spectral resolution of 4 cm^{-1}. The UV-Vis and Vis-Diffuse reflectance (V-DR) spectra were recorded by using a Shimadzu UV-2600 spectrophotometer. $BaSO_4$ was used as a reference in the V-DR measurements. The fluorescence spectra were measured in solution by using a Shimadzu RF-6000 instrument and in solid state were carried out with an Agilent Cary Eclipse fluorescence spectrophotometer. TG and DT analyses were performed by using Shimadzu TG-50 and DT-50 units from room temperature up to 800 ºC at a heating rate of 5 ºC min^{-1} and oxygen flow of 50 mL min^{-1}.

2.2.1 Antibacterial activity

The antibacterial activity of the complexes has been tested against Gram-negative and Gram-positive bacteria by using the Kirby-Bauer agar diffusion method [18]. The bacteria strains were obtained from the American Type Culture Collections (ATCC). *Escherichia coli* (ATCC 8739), *Salmonella typhimurium* (ATCC 14028), *Staphylococcus aureus* (ATCC 49775) and *Bacillus cereus* (ATCC 10987) have been used. For all the strains, Nutrient agar and Mueller Hinton agar were used as the cultivation and assay medium, respectively. Stock aqueous solutions (20 mg ml^{-1}; 6 % DMSO) of the compounds were prepared and sterilized by filtration using 0.45 µm Millipore filters (Acrodisc nylon membrane). A suspension of each activated microorganism was prepared and adjusted by comparing with a 0.5 McFarland standard (~$1.5x10^8$ bacteria per ml) [19,20], before seeding it on the assay agar. After the seeding of the bacteria, MN 827 ATD disks (6 mm in diameter) were impregnated with the compounds and placed over the inoculated agar. A disk with 6% DMSO solution was used as a negative control, as well as Tego51® was used as a positive control. To accomplish a better diffusion of the compounds, the inoculated agar was kept at 4 ºC for 3 h, and then the plates were incubated at 37 ºC for 24 h. All the assays were carried out three times.

2.2.2 Singlet Oxygen Generation and Fluorescence Quantum Yields

The singlet oxygen (O_2 ($^1\Delta_g$)) quantum yield (Φ_Δ) is an indicator of the capacity of a substrate to generate singlet oxygen mainly from its triplet state [21]. This property is defined as the number of molecules of O_2 ($^1\Delta_g$) generated per each absorbed photon by a photosensitizer. The irreversible photooxygenation of 9,10-dimethylanthracene (DMA; an efficient O_2 ($^1\Delta_g$) quencher) was used as an indirect measurement of the produced singlet oxygen. Rose Bengal (RB) was employed as a reference photosensitizer. All the experiments were carried out at 25 ºC, in quartz cells (10 mm optical pathway) and under continuous stirring. The radiation light (3000 Å Rayonet UV lamps) was filtered with basic potassium dichromate solution to selectively irradiate the photosensitizer

View Article Online
DOI: 10.1039/C8NJ00661J

without irradiating the DMA. All the experiments were performed in triplicate and the Φ_Δ values were calculated following the equation 1.

$$\phi_{\Delta,x} = \phi_{\Delta,RB}\left(\frac{k_x}{k_{RB}}\right) \quad (1)$$

Where the subscripts *x* and RB denote problem sample and Rose Bengal, respectively; Φ_Δ is the yield of singlet oxygen production ($\Phi_{\Delta,RB}$ = 0.68, in ethanol) [21] and *k* is the experimental first-order kinetic constant for the consumption of DMA by $^1O_2$. The *x* and RB absorbances were matched at 318 nm.

The fluorescence quantum yields were measured by using a comparative methodology [22] with quinine sulfate as a reference fluorophore. First, 0.02 M stock solutions of quinine sulfate (0.05 M H_2SO_4), 6-MeOQ and complexes **I - V** (absolute ethanol) were prepared. Afterward, the fluorescence spectra (PL; λ_{exc} = 310 nm) of dilutions with absorbances lower than 0.2 units at 310 nm were recorded. Next, the PL spectra were numerically integrated from 320 to 600 nm by using the software GNU Octave [23]. Finally, the fluorescence quantum yields were calculated following the equation 2.

$$\phi_{f,x} = \phi_{f,Q}\left(\frac{S_x}{S_Q}\right)\left(\frac{\eta_x^2}{\eta_Q^2}\right) \quad (2)$$

Where the subscripts *x* and Q denote problem sample and quinine sulfate, respectively; Φ_f is the quantum yield of fluorescence ($\Phi_{f,Q}$ = 0.546) [24], S is the gradient from the plot of integrated fluorescence intensity vs. Abs, and η the refractive index of the solvents ($\eta_{H2SO4\ (0.05\ M)}$ = 1.34 and η_{EtOH} = 1.361).

2.3 X-ray data collection and Structure refinement

The data for the complexes were collected on an Agilent Gemini Diffractometer with an EOS CCD detector equipped with a graphite-monochromated Mo Kα (λ = 0.71073 Å) and Cu Kα (λ = 1.54184 Å) radiation. X-ray diffraction intensities were collected (ω scans with θ and κ-offsets), integrated and scaled with CrysAlisPro [25] suite of programs. The unit cell parameters were obtained by least-squares refinement (based on the angular settings for all collected reflections with intensities larger than seven times the standard deviation of measurement errors). Data were corrected empirically for absorption employing the multi-scan method implemented in CrysAlisPro (Agilent Technologies Ltd., Yarnton, Oxfordshire, UK). The structures were solved by direct methods with SHELXS-97 (Göttingen, Lower Saxony, Germany) [26] and the molecular models refined by the full-matrix least-squares procedure on F^2 with SHELXL-97 [27,28]. All hydrogen atoms were located from a Fourier difference map phased on the heavier atoms and refined at their found positions with isotropic displacement parameters. However, those of the Ag complex were positioned stereochemically and refined riding on the bound atoms with isotropic displacement parameters. Hydrogen atoms of the methyl groups in Co and Ni complexes were restrained to its idealized geometry by treating C-H bond lengths and H···H distances to a target value of 0.96(1) and 1.57(2) Å, respectively. Crystal data and refinement results are summarized in Table 1. CIF files with details of the crystal structures reported in this paper have been deposited with the Cambridge Crystallographic Data Centre, under deposition numbers CCDC 1814014 - 1814018 (See table 1).

Table 1. Crystal data and structure refinement for the complexes.

Compound	**I**	**II**	**III**	**IV**	**V**
Empiric formula	$CoC_{20}Cl_3N_2O_2H_{19}$	$NiC_{20}Cl_2N_2O_2H_{18}$	$CuC_{20}Cl_2N_2O_2H_{18}$	$ZnC_{20}Cl_2N_2O_2H_{18}$	$AgC_{20}N_3O_5H_{18}$
CCDC deposition code	1814017	1814016	1814014	1814018	1814015
Formula weight	484.65	447.97	452.82	454.66	488.24
Temperature [K]	297(2)	297(2)	297(2)	297(2)	297(2)
Wavelength [Å]	0.71073	0.71073	1.54184	0.71073	1.54184
Crystal system	Triclinic	Monoclinic	Monoclinic	Monoclinic	Monoclinic
Space group	*P*-1	$P2_1/c$	$P2_1/n$	$P2_1/c$	$P2_1/n$
Unit Cell dimensions [Å, °]					
a	7.4148(3)	10.3725(4)	4.7645(3)	10.3857(4)	7.3869(2)
b	9.4514(4)	15.1031(6)	12.5214(6)	15.2082(6)	15.0294(5)
c	15.8456(9)	12.5383(4)	16.2924(8)	12.5660(6)	17.1175(5)
α	104.570(4)				
β	91.426(4)	91.770(3)	96.847(5)	91.344(4)	98.470(3)
γ	104.966(8)				
Volume [$Å^3$]	1033.33(8)	1963.27(13)	965.04(9)	1984.23(14)	1879.67(10)
Z, Density (calculated) [g cm^{-3}]	2, 1.558	4, 1.516	2, 1.556	4, 1.522	4, 1.725
Absorption coefficient	1.237	1.278	4.293	1.524	8.948

View Article Online
DOI: 10.1039/C8NJ00661J

[mm^{-1}]					
F(000)	494	920	462	928	984
Crystal size [mm]	0.033×0.081×0.359	0.190×0.227×0.503	0.020×0.027×0.215	0.136×0.235×0.321	0.043×0.045×0.372
θ range for data collection [°]	2.97 ≤ θ ≤ 29.18	3.25 ≤ θ ≤ 29.18	7.07 ≤ θ ≤ 72.12	3.13 ≤ θ ≤ 29.56	3.933≤θ≤73.397
Index ranges	-10 ≤ h ≤ 9 -12 ≤ k ≤ 12 -16 ≤ l ≤ 20	-13 ≤ h ≤ 12 -17 ≤ k ≤ 19 -16 ≤ l ≤ 16	-5 ≤ h ≤ 5 -11 ≤ k ≤ 15 -20 ≤ l ≤ 18	-14 ≤ h ≤ 14 -19 ≤ k ≤ 18 -12 ≤ l ≤ 16	-8 ≤ h ≤ 8 -15 ≤ k ≤ 18 -20 ≤ l ≤ 21
Reflections collected / unique	8344/4698 [R(int) = 0.0275]	9827/4529 [R(int) = 0.0253]	3026/1820 [R(int) = 0.0280]	17617/4850 [R(int) = 0.0528]	7973/3681 [R(int) = 0.0272]
Completeness to θ [%]	84.2 (29.18º)	85.3 (29.18º)	95.8 (72.12º)	99.8 (25.242°)	100.0 (67.684°)
Absorption correction	Semi-empirical from equivalents				
Max. / min. transmission	1.00000/0.95527	1.00000 / 0.90687	1.00000 / 0.98222	1.00000 / 0.65788	1.00000 / 0.64050
Refinement method	Full-matrix least-squares on F^2				
Data/restraints/parameters	4698 / 12 / 329	4529 / 12 / 316	1820 / 0 / 161	4850 / 0 / 304	3681 / 0 / 263
Goodness-of-fit on F^2	1.024	1.040	1.056	1.063	1.117
Final R indices [I > 2σ(I)]	R1=0.0375, wR2=0.0776	R1= 0.0363 wR2= 0.0754	R1=0.0422 wR2=0.1068	R1=0.0482 wR2=0.1144	R1=0.0545 wR2= 0.1444
R indices (all data) [a]	R1=0.0572 wR2=0.0860	R1= 0.0560 wR2= 0.0861	R1=0.0549 wR2=0.1170	R1=0.0755 wR2=0.1346	R1=0.0675 wR2=0.1516
Largest diff. peak / hole [e.$Å^{-3}$]	0.281 / -0.279	0.252 / -0.358	0.395 / -0.309	0.764 / -0.292	1.030 / -0.913

[a] $R1=\Sigma||F_o|-|F_c||/\Sigma|F_o|$, $wR2=[\Sigma w(|F_o|^2-|F_c|^2)^2/\Sigma w(|F_o|^2)^2]^{1/2}$

2.4 Hirshfeld surface calculations

The Hirshfeld surface analysis is a tool for visualizing and quantifying the intermolecular interactions in crystalline systems. The Hirshfeld surfaces of the complexes and their respective 2D fingerprint plots were calculated with the aid of the CrystalExplorer 17.5 software at *very high* resolution [29–31]. The d_{norm} plot considers the distances to the surface from nuclei outside and inside the Hirshfeld surface (d_e and d_i, respectively). The d_{norm} surface is plotted over a fixed color scale of -0.25 au (red) – 0.95 Å au (blue). Shape index plot is mapped in the color range -1.0 au (concave) 1.0 au (convex) and the curvedness plot in the range of -4.0 au (flat) – 0.4 (singular). The 2D fingerprint plots were displayed in the 0.5 - 2.8 Å range, and including reciprocal contacts. 2D Difference Hirshfeld fingerprint plots were calculated following the methodology and codes written by Carter *et al.* (*fingerprint - Fortran90* and *plot_ finger - C*) [32]. Although 2D Difference Hirshfeld fingerprint plots were originally developed for the analysis of polymorphic crystals, we have found them very useful in the characterization of isostructural compounds where only subtle differences can be evidenced. The 3D surfaces were plotted using the CrystalExplorer 17.5 software, while the 2D fingerprint plots were visualized using the freely distributed Gnuplot Software [33].

3. Results and Discussion

3.1 Crystal structure analysis

Crystal structures were not reported for the already published Cu(II) and Zn(II) complexes [7] but their coordination spheres have been properly proposed in agreement to our results. However, the authors reported the Co(II) and Zn(II) complexes as isostructural. According to our X-ray diffraction results for **I,** this complex consists of an ionic pair, with a tetrahedrally coordinated metal center. The Cobalt atom is surrounded by one N and three chlorines in the anion ($CoNCl_3$). A 6-methoxyquinolinium act as the cation. The isostructural Ni(II) and Zn(II) complexes are tetrahedrally coordinated and the metals are located in a MN_2Cl_2 coordination sphere (Figure S3). In **III** the cation is located at a CuN_2Cl_2 coordination sphere forming a centrosymmetric square planar environment. Finally, the Ag(I) center is two-coordinated in a distorted AgN_2 linear environment and interacts with an oxygen atom from the nitrate anion at 2.7215(1) Å.

Selected bond and angles around the central cations are summarized in Table 2, and the coordination spheres with the used labels are shown in Figures 1, 2 and S1 for all complexes.

Table 2. Selected bond lengths (Å) and angles (°).

	I [a]	II	III [b]	IV	V
M–N	2.0747(1)	2.0232(1) / 2.0268(1)	2.0110(1)	2.0724(1) / 2.0682(1)	2.165(5) / 2.151(5)
M–Cl	2.2691(1) / 2.2661(1) / 2.2379(1)	2.2424(1) / 2.2364(1)	2.2490(1)	2.2418(1) / 2.2304(1)	
Ag···ONO_2 [v]					2.7215(1)

Ag···Ag^{v}					3.3405(1)
N–M–N		101.05(1)	180.00	103.15(1)	159.55(1)
Cl–M–Cl	109.80(1) / 110.22(3) / 111.14(3)	119.69(1)	180.00	114.92(1)	
N11–M–Cl	103.63(6) / 103.38(5) / 118.15(1)	107.56(5) / 111.31(5)	90.38(7)	110.95(7) / 106.40(7)	
N21–M–Cl		109.49(5) / 106.13(6)		107.53(7) / 113.26(7)	

[a] In **I** the Co(II) atom is coordinated to one 6-MeOQ ligand and three chlorine atoms, see text for further details. [b] In **III** the Cu(II) atom is located at an inversion center. Roman superscripts denote symmetry operations: see Figure 1.

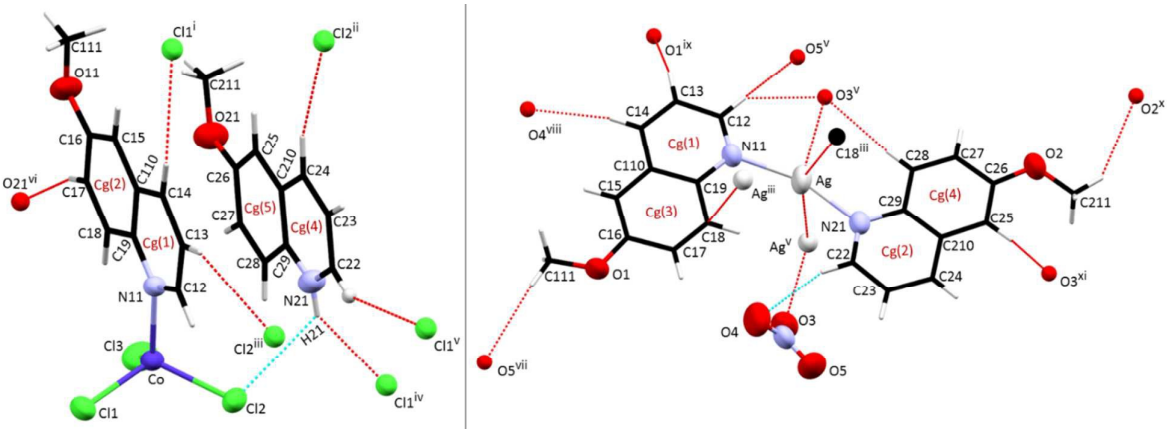

Figure 1. Molecular structure of ionic **I** (left) and **V** (right). Inter and intramolecular interactions are depicted as red and light blue dashed lines, respectively. Symmetry Operations: i) *x*, -1+*y*, *z*; ii) -1+*x*, -1+*y*, *z*; iii) 1-*x*, -*y*, -*z*; iv) -1+*x*, *y*, *z*; v) -*x*, -*y*, -*z*; vi) 1-*x*, 1-*y*, 1-*z*; vii) ½-*x*, -½-*y*, ½+*z*; viii) -½+*x*, -½-*y*, ½+*z*; ix) ½-*x*, ½+*y*, -½-*z*; x) -*x*, -*y*, 1-*z*; xi) ½-*x*, -½+*y*, ½-*z*.

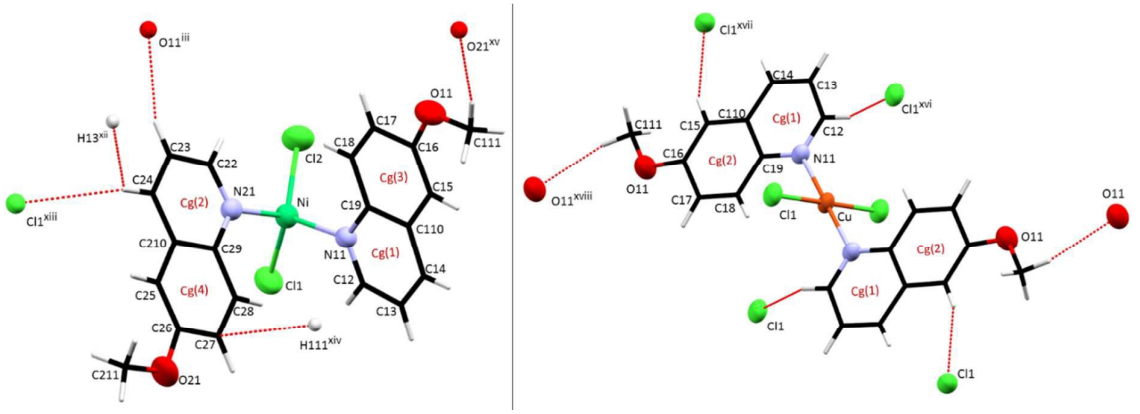

Figure 2. Molecular structure of **II** (left) and **III** (right). Intermolecular interactions are depicted as red dashed lines. Symmetry Operations: iii) 1-*x*, -*y*, -*z*; xii) 1+*x*, *y*, *z*; xiii) 1-*x*, -*y*, 1-*z*; xiv) *x*, ½-*y*, ½+*z*; xv) *x*, *y*, 1+*z*; xvi) -*x*, 1-*y*, 1-*z*; xvii) ½-*x*, ½-*y*, ½-*z*; xviii) 2-*x*, 1-*y*, -*z*; xix) 2-*x*, ½+*y*, ½-*z*; xx) 2-*x*, -*y*, 1-*z*.

The degree of distortion of the coordination polyhedra with respect to ideal four and two vertex polyhedra was estimated using the SHAPE software [34] which considers the continuous shape measure theory. The results for **I**, **II** and **IV** indicated that the metallic centers are in the deviation pathway between the Tetrahedron (T-4) and the axially vacant trigonal bipyramid (vTBPY-4), being much better described by the T-4 environment. The environment of **III** is very close to the Square (SP-4) geometry. Finally, the results for **V** indicated that the Ag(I) cation is located between the Linear (L-2) and the Divacant tetrahedron (vT-2; V-shape, 109.47º) geometries, being closer in shape to L-2. The calculated values are listed in the Tables S1 and S2 (ESI).

View Article Online
DOI: 10.1039/C8NJ00661J

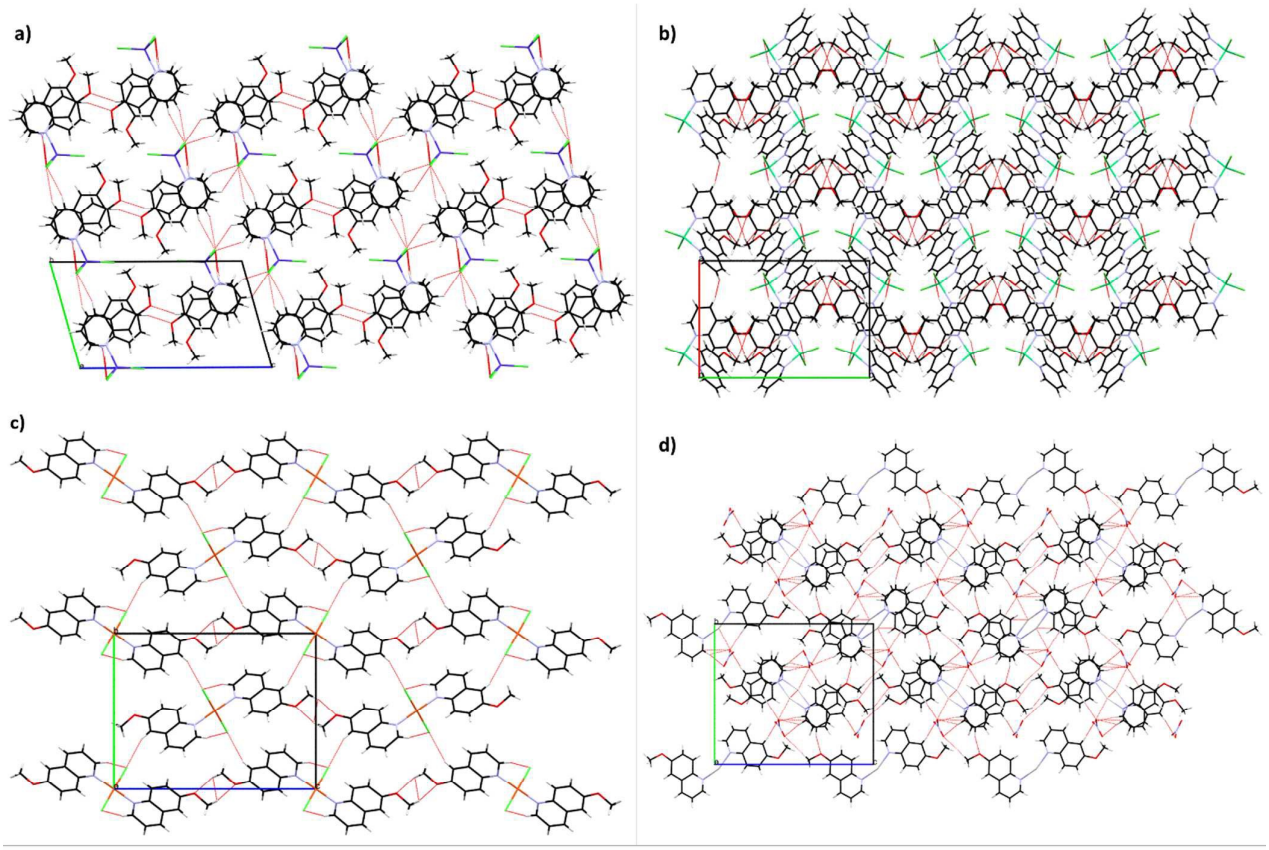

Figure 3. Packing schemes of **I, II, III,** and **V** (a - d, respectively). Views along [100] for **I**, **III** and **V**, and [001] for **II**. Intra and intermolecular contacts are depicted by red dashed lines.

Different supramolecular assemblies constructed through different kind of intermolecular interactions are shown in Figures 3 and S4 for all complexes. In **I**, the protonated 6-MeOQ moiety is linked to two contiguous $CoNCl_3$ anions through a bifurcated N—H···Cl hydrogen bond developing infinite chains of Cl2···H21···Cl1^{iv} type along the *a*-axis (see Figure S2). Besides, this hydrogen bond is assisted by a π··· π interaction established between the rings of 6-MeOQ moieties belonging to the cation and the anion. The arrangement observed for complexes **II** and **IV** are similar and the π ··· π stacking interactions play an important role in their crystal lattices. Additionally, in both crystal structures, C—H···Cl, C—H···O and C—H···C interactions are involved in the crystal lattice (see Figures 3 and S4, and Table 3).

In the supramolecular assembly of **III**, infinite chains are formed by Cl2—H12···Cl1^{xvi} and Cg(1) ··· Cg(2)^{iv} (π-stacking) interactions arranged parallel to the *a*-axis. Each of them also interacts with the neighboring chains via C15—H15···Cl1^{xvii} (see Tables 3 and 4 below). In complex **V** the two 6-MeOQ moieties coordinated to the Ag(I) center, are oriented along the [1,0,1] crystallographic direction developing infinite chain stabilized by C—H···O hydrogen bond and likely by Van der Waals interactions between methoxy groups related by inversion centers. Along *b*-axis, infinite chains, related by two-fold screw axis, pack through C—H···O hydrogen bonds, involving 6-MeOQ ring and oxygen atoms from the methoxy and nitrate groups, developing neutral [1,0,1] layers (see Table 3). Finally the 3D structure is developed by the packing of these layers along the *a*-axis through π ··· π stacking interactions of the 6-MeOQ rings and an argentophilic interaction between silver centers [35,36] (Ag···Ag^{v} at 3.3405(1) Å; Fig. 1). Beside the Ag-center also interacts with the C18^{iii} at 3.3132(1) Å (Fig.1). For further information about the main π ··· π interactions in the complexes see Table S3.

Table 3. Intra and intermolecular hydrogen bonds for the complexes [Å and °]. Data obtained with the Platon Software.

	D—H···A	D—H	H···A	D···A	∠ D—H···A	Label (See Fig. 4)
I	C13—H13···Cl2^{iii}	1.00	2.89	3.6478(2)	133	1
	C17—H17···O21^{vi}	0.93	2.41	3.3031(2)	161	3
	N21—H21···Cl2^{intra}	0.86	2.88	3.4511(2)	126	4
	N21—H21···Cl1^{iv}	0.86	2.44	3.1817(2)	145	5

View Article Online
DOI: 10.1039/C8NJ00661J

	C22—H22···Cl1^{v}	0.93	2.78	3.6127(2)	150	6
II	C111—H113···O21^{xv}	0.96	2.64	3.5944(1)	170	1
	C23—H23···O11^{iii}	0.93	2.55	3.4322(1)	158	2
	C13—H13···Cl2^{xxi}	0.95	2.95	3.6401(1)	130	3
	C28—H28···Cl1^{intra}	0.95	2.84	3.5697(1)	134	
	C22—H22···Cl2^{intra}	0.91	2.73	3.4063(1)	132	
	C18—H18···Cl2^{intra}	0.92	2.74	3.5022(1)	141	
	C12—H12···Cl1^{intra}	0.92	2.78	3.4487(1)	131	
III	C12—H12···Cl1^{xvi}	0.93	2.71	3.5503(2)	151	1
	C15—H15···Cl1^{xvii}	0.90	2.77	3.6298(2)	158	2
	C111—H111A···O11^{xviii}	1.00	2.62	3.5988(2)	165	3
IV	C111—H113···O21^{xv}	1.02	2.73	3.6140(6)	171	1
	C23—H23···O11^{xiii}	0.94	2.59	3.4507(2)	152	2
	C13—H13···Cl2^{xix}	0.91	2.93	3.6100(2)	133	3
	C22—H22···Cl2^{intra}	0.92	2.76	3.4513(2)	133	
	C12—H12···Cl1^{intra}	0.90	2.84	3.4864(2)	130	
	C18—H18···Cl2^{intra}	0.87	2.85	3.5939(2)	145	
	C12—H12···O5^{v}	0.93	2.66	3.5536(1)	160	1
	C12—H12···O3^{v}	0.93	2.39	3.1573(1)	140	2
V	C13—H13···O1^{ix}	0.93	2.57	3.3588(1)	143	3
	C14—H14···O4^{viii}	0.93	2.46	3.3749(1)	167	4
	C111—H11A···O5^{vii}	0.96	2.68	3.4630(1)	162	5
	C22—H22···O4^{intra}	0.93	2.53	3.3299(1)	144	6
	C25—H25···O3^{xi}	0.93	2.60	3.3812(1)	142	7
	C211—H21A···O2^{x}	0.96	2.66	3.4826(1)	143	8
	C28—H28···O3^{v}	0.93	2.45	3.3526(1)	164	9

For Symmetry codes see Figures 1 and 2.

3.2 Hirshfeld Surface analysis

Hirshfeld surface analysis was performed with the aim of studying the nature of the intra and intermolecular interactions and their contribution to the supramolecular assembly of the complexes. The d_{norm} Hirshfeld surfaces for all complexes are shown in Figures 4 and S5. In the d_{norm} surface of **I,** the H17···O21^{vi} and H12···Cl1^{iv} interactions are observed as deep red spots labeled as 3 and 5, respectively. Further weak H···Cl contacts are evidenced as light red zones (labels 1, 2, 4, 6 and 7). The 3D arrangements in **II** and **IV** are quite similar between them. In their d_{norm}, the most important contributions correspond to C—H···O, C—H···Cl and dihydrogen C—H···H interactions (labels 2, 3 and 4, respectively). Besides, in both complexes a weaker C—H···O interaction involving the methoxy H and O-atoms is observed (label 1; see also Fig.2). The d_{norm} surface of **III** shows two different H···Cl interactions indicated as red spots. The first of them, C12—H12···Cl1 participates in the formation of chains through the *a*-axis as previously discussed. On the other hand, the C15—H15···Cl1 contact acts as a link between those neighboring chains. Furthermore, weak C111—H111A···O11 interaction are observed in this plot. Lastly, in the d_{norm} surface of complex **V**, the most important interactions are those that involve cation···anion interactions. C12—H12···O5^{v}, C12—H12···O3^{v}, C28—H28···O3^{v} and Ag···O3^{v} (labels 1, 2, 9 and 10). Moreover, an argentophilic Ag···Ag^{v} (label 11) and a Ag···C18^{iii} (labeled as 12) interactions are observed. Further several C—H···O weak interactions are visualized for this complex (labels 3, 4, 5, 6 and 8). For more details about the geometric parameters of these interactions see Table 3.

View Article Online
DOI: 10.1039/C8NJ00661J

NJC

ARTICLE

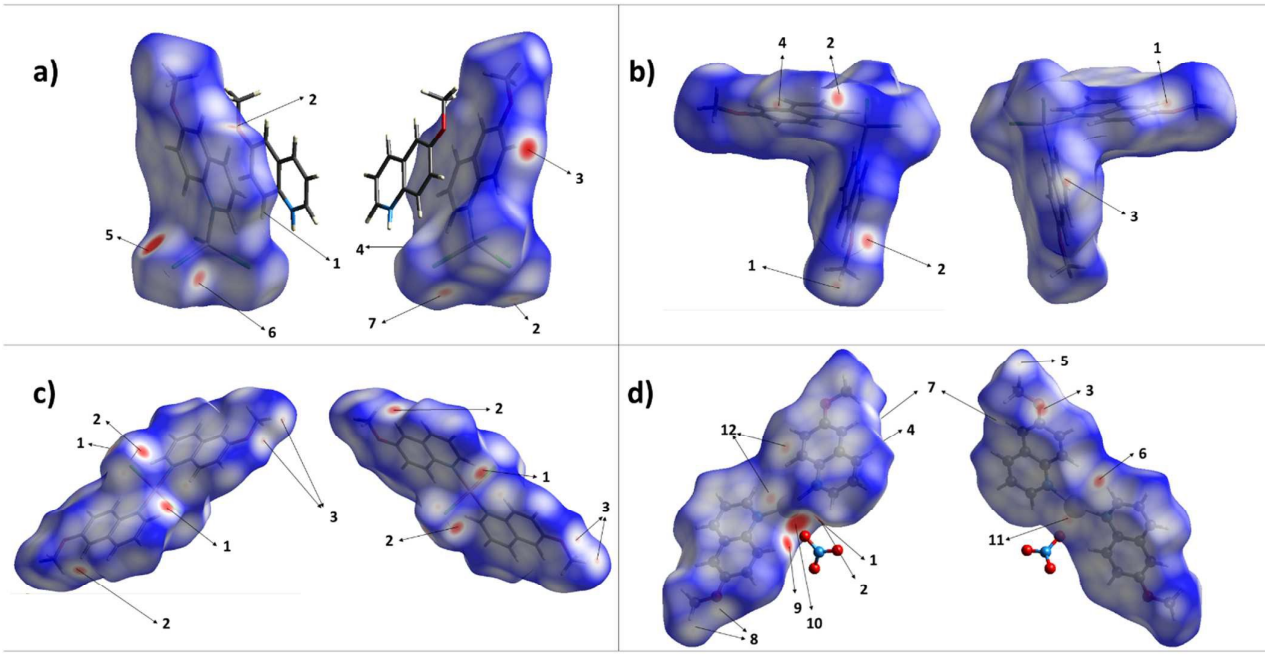

Figure 4. Views of the d_{norm} Hirshfeld surfaces in two orientations for **I**, **II**, **III,** and **V** (a - d, respectively). Numbered arrows are described either in Table 2 or the text.

The 2D fingerprint plots are useful in the quantification of different interactions. The fingerprint plots of the compounds are shown in Figure 5. For **I**, the O···H interactions are the shortest with a $d_e + d_i$ distance of ~ 2.26 Å, and a 6.6 % contribution to the total Hirshfeld surface. Then, the dihydrogen interactions at a $d_e + d_i$ distance of ~ 2.3 Å play the most important contribution to the total Hirshfeld surface with a 39.2 %. The Cl···H contacts at $d_e + d_i \approx 2.31$ Å have a slightly lower contribution (38.3 %) to the total surface than H···H contacts. Finally, the π ··· π contacts are evidenced as a light blue zone at $d_e + d_i \approx 3.62$ Å (6.3 % C···C + 1.0 % C···N).

The fingerprint plots of **II** and **IV** are very similar (Figures 5b and 5d). The H···H contacts are the shortest at a $d_e + d_i$ distance of ~ 2.08 Å. At the same time, these interactions present the mayor contribution to the total Hirshfeld surface (37.8 and 38.6 %, for **II** and **IV**, respectively). Besides, C···H (~ 2.8 Å), O···H (~ 2.4 Å) and C···O (~ 3.2 Å) interactions also contribute significantly to the surfaces (C···H: 17.2 and 17.0 %; O···H: 6.5 and 5.9 % for **II** and **IV,** respectively, and C···O: 3.5% for both). The Cl···H interactions ($d_e + d_i \approx 2.8$ Å) also play an important role in the total surface with 23.6 and 23.7 % contribution for **II** and **IV**, respectively. The π ··· π contacts are observed in the same way than in I ($d_e + d_i \approx 3.7$ Å). Lastly, in these complexes, a small contribution (~1.0 %) from M···H interactions is observed at $d_e + d_i \approx 3.0$ Å (M = Ni or Zn).

View Article Online
DOI: 10.1039/C8NJ00661J
NJC ARTICLE

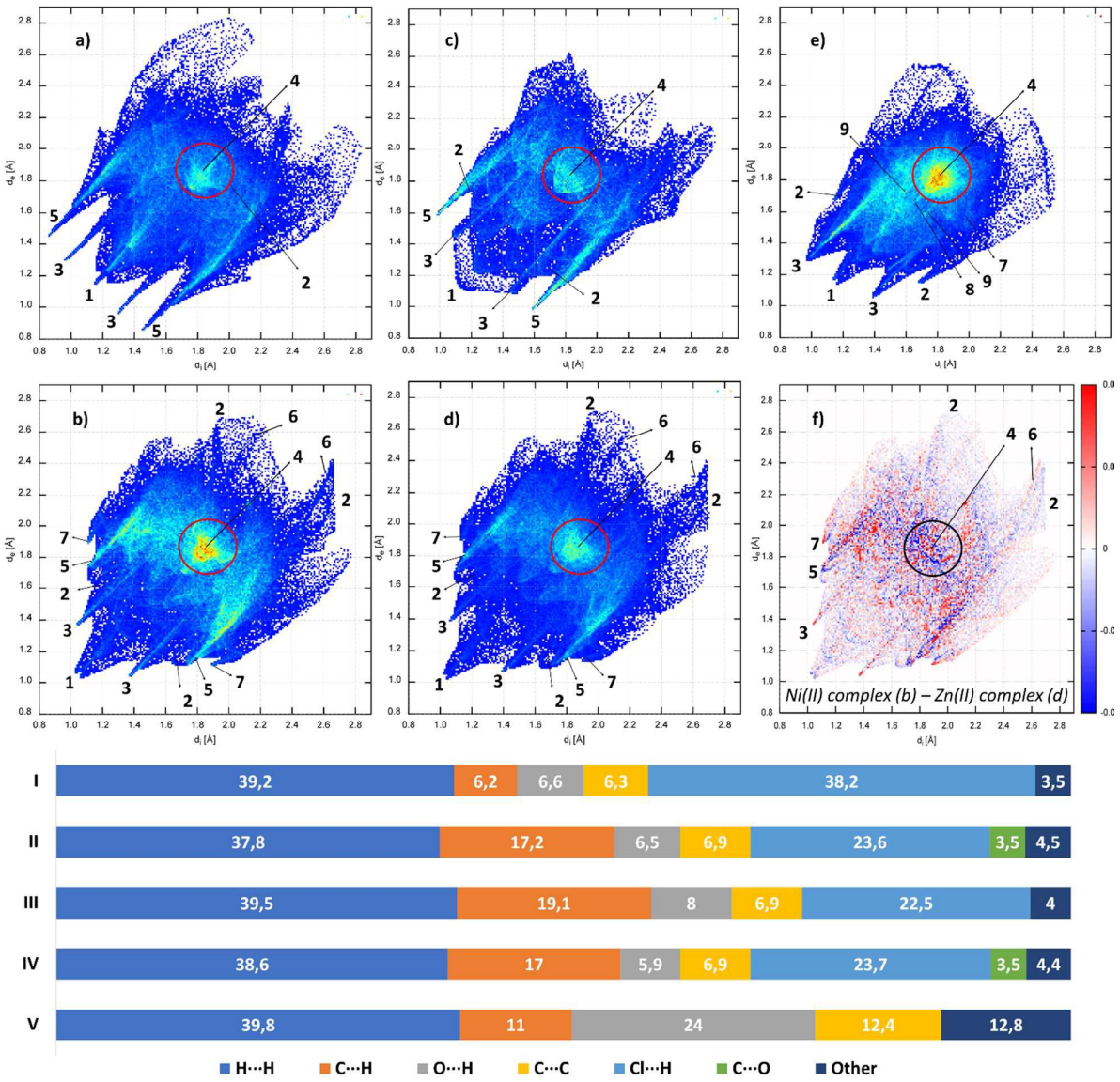

Figure 5. Top: Fingerprint plots for compounds **I - V** (a - e, respectively) and (f) the difference fingerprint for isostructural **II** and **IV** complexes. Close contacts are labeled as (1) H···H, (2) C···H, (3) O···H, (4) C···C, (5) Cl···H, (6) C···O, (7) M···H, (8) Ag···Ag and (9) Ag···C. Bottom: Relative contributions of the intermolecular interactions to the Hirshfeld surface for the compounds [%]; values lower than 2 % were included in other.

To compare the relative intermolecular interactions between **II** and **IV**, a difference fingerprint plot [32] was calculated (Figure 5f). Only slight differences were observed. In **II**, O···H, C···O and M···H interactions are more significative in the crystal lattice. While in **IV**, the C···H and Cl···H interactions play a greater role than in **II**. The other interactions are similar in both complexes.

The fingerprint plot of **III**, reveals that the shortest interactions are H···H ($d_e + d_i \approx 2.26$ Å), O···H ($d_e + d_i \approx 2.54$ Å) and Cl···H ($d_e + d_i \approx 2.58$ Å), which have contributions of 39.5, 8.0 and 22.5%. Other significative features are the C···H (~ 2.96 Å) and the C···C (~ 3.62 Å) contacts with a contribution of 19.1 and 6.9%, respectively. Lastly, in compound **V**, the closer interactions are the H···H ($d_e + d_i \approx 2.3$ Å), O···H ($d_e + d_i \approx 2.26$ and 2.44 Å) and C···H ($d_e + d_i \approx 2.83$ Å). These interactions participate in the total Hirshfeld surface with contributions of 39.8, 24.0 and 11.0 %. The C···C contacts ($d_e + d_i \approx 3.62$ Å; 12.4 %) also play an important role in the assembly. Besides, the presence of some interactions in which the Ag-atom participates is evidenced in the fingerprint of this complex, for example Ag···H (2.1 %), Ag···C ($d_e + d_i \approx 3.28$ Å; 1.2 %), Ag···Ag ($d_e + d_i \approx 3.34$ Å; 0.8 %) and Ag···O ($d_e + d_i \approx 2.71$ Å; 0.8 %)).

View Article Online
DOI: 10.1039/C8NJ00661J

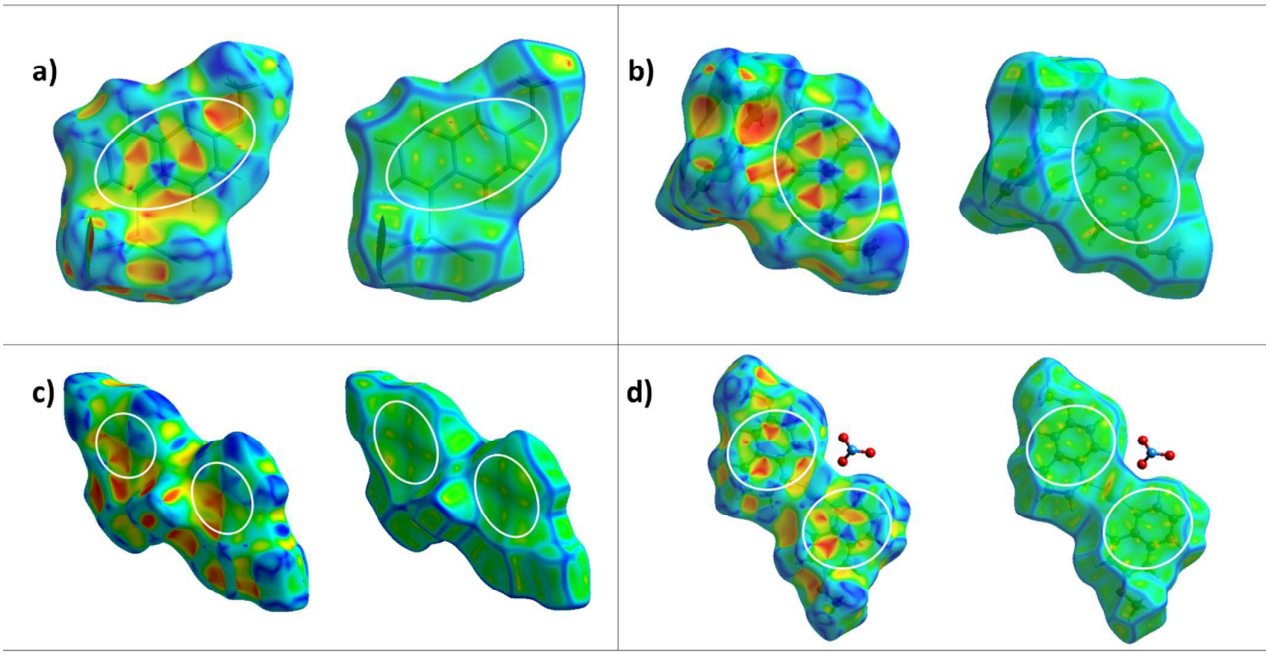

Figure 6. Hirshfeld surfaces mapped with *shape-index* and *curvedness* for **I**, **II**, **III,** and **V** (a - d, respectively). In **I** the cation has been removed for clarity.

The *Shape-index* and *curvedness* can be plotted over the Hirshfeld surfaces (Figure 6 and S6). These plots are particularly useful in compounds with π ··· π interactions. This kind of interaction is evidenced in the *shape-index* plot as a red and blue "triangles" pattern and in the *curvedness* plot by a flat region in the same zone of the surface. In **I - V**, π ··· π interactions play an important role in the 3D assemblies of the compounds. Figure 6 shows the previously described features within white ellipses. The π ··· π interactions are established between 6-MeOQ rings of neighboring molecules. (For further information see Table S3).

3.3 Spectroscopic properties

3.3.1 Fourier Transform Infrared Spectroscopy (FTIR)

The vibrational features of compounds **I**, **III** and **IV** have been previously discussed [7]. The most relevant infrared bands of the **II** and **V** are given in Table 4, and the spectra are presented in Figure S7. The band attributed to the O—CH_3 stretching is observed at 1230 cm^{-1} in the free ligand. In both complexes, this feature is slightly shifted in agreement with the previously discussed intermolecular interactions. However, the bands assigned to ring vibrations (1572 and 1500 cm^{-1}) were shifted to higher wavenumber after complexation according to the N-donor coordination with the metal center. In complex **V**, an additional band is observed at 1384 cm^{-1}, which is assigned to the stretching mode of the nitrate anion.

Table 4. Selected features from the FTIR spectra [cm^{-1}].

Compound	Ring Vibrations	ν (C — O)	ν (NO_3)	
6-MeOQ	1572	1500	1230	
II	1594	1512	1236	
V	1596	1585	1234	1384

3.3.2 Electronic Spectroscopy

The normalized UV-Vis (ethanol), Vis-DR ($BaSO_4$) and fluorescence (ethanol) spectra for complexes **I - V** are displayed in Figure S8. In all the complexes, the bands observed at wavelengths lower than 400 nm are due to the intraligand transitions. Furthermore, for **I**, **II** and **III** new bands are observed in the visible range of the spectra. Two bands are observed in the Vis-DR spectrum of **I** at 512 and 635 nm, while in the spectrum of **II** is evidenced a broad band centered at 575 nm. Those features agree with the d-d transitions expected for the tetrahedral environments around the d^7 Co(II) and d^8 Ni(II) cations. The Vis-DR spectrum of **III** shows three bands at 548, 626 and 692 nm, in agreement with the d-d transitions typical for a d^9 Cu(II) ion in a square planar environment. No d - d transitions were observed for **IV** and **V**, as expected from their d^{10} electronic configuration.

The fluorescent emission of the ligand has been previously characterized[2]. The authors found that in acid medium, the N-atom is protonated, and the emission maximum is centered at 438 nm, while it is unprotonated at neutral or basic medium, and the maximum is at 362 nm. In our case, the fluorescence spectra of the complexes in solution are very similar to that of the ligand at neutral pH. The spectra show an emission maximum centered at 355 nm, suggesting that the photoluminescence can be assigned to the intraligand fluorescence processes. In the solid state (Figure S9)

View Article Online
DOI: 10.1039/C8NJ00661J

the spectra of complexes **I** and **III** display several features in the 325 - 575 nm spectral range after excitation at 254 nm. In both cases the fluorescence intensity is lower than in the complex **IV** spectrum, which can be attributed to the expected fluorescence quenching by semi-full d shell transition metals [37] (*vide infra*). The spectrum of **IV** displays a broad band centered at 425 nm. In the spectra of the three complexes is observed a marked red-shift as compared with the solution measurements.

3.4 Singlet Oxygen and Fluorescence Quantum Yields

The singlet oxygen generation quantum yields were measured using steady-state techniques by following the consumption of DMA by $^1O_2$ (See Figure S10). Upon coordination, a decrease in the singlet oxygen yield for all the compounds was observed (see Table 5). This decrease is probably associated with the life time excited triplet diminution which could be attributed to bonding and no bonding interactions [38,39].

However, the Φ_Δ values found for the complexes are similar or even higher than those of some reported transition metal complexes of Co(II), Ni(II), Cu(II) , Zn(II) and Ru(II) complexes with different ligands (Φ_Δ = 0.32, 0.27, 0.30, 0.40 and 0.29, respectively) [21,40,41].

The fluorescence of a ligand is often quenched by transition metals after complexation. This common phenomenon is attributed to different processes such as redox activity, magnetic perturbances, electronic transfer, etc. [37,42,43]. However, it is desirable that the fluorescence quantum yield of the coordination compounds be at least the same or higher than that of the free ligand. In these cases, the complexes could be used in photochemical applications (*e.g.,* light emitting devices, fluorescent probes). The fluorescence quantum yields of the complexes were calculated following equation 2. The results are very close to that of the ligand, indicating that there is not significative contribution of the above-mentioned quenching processes. The values are listed in Table 5, and the plots of integrated fluorescence are displayed in Figure S11. These values are similar to those of Al(III), Zn(II) and Mg(II) with salen ligands (0.18, 0.14 and 0.19, respectively) [44] and they are considerably higher than those for Zn(II), Cd(II) and Sn(IV) complexes with different ligands (~10^{-3} in all the cases) [45,46].

Table 5. Experimental kinetic constants for the DMA consumption by $^1O_2$ in presence of the free ligand and complexes **I - V** (k_x, [min^{-1}]) [a], $^1O_2$ ($^1\Delta_g$) production quantic yields (Φ_Δ) [b], slope of the curves of integrated fluorescence vs Absorbance [c] and fluorescence quantic yields (Φ_f) [d].

Comp.	k_x x 10^3	Φ_Δ	S_x x 10^{-7}	Φ_f
I	4.06 ± 0.07	0.468 ± 0.005	2.53 ± 0.07	0.122 ± 0.007
II	2.49 ± 0.03	0.287 ± 0.004	3.24 ± 0.08	0.156 ± 0.009
III	4.32 ± 0.06	0.498 ± 0.007	2.99 ± 0.08	0.145 ± 0.009
IV	5.12 ± 0.05	0.590 ± 0.010	3.24 ± 0.14	0.156 ± 0.028
V	2.69 ± 0.14	0.310 ± 0.030	3.30 ± 0.09	0.159 ± 0.011
6-MeOQ	-	0.94 ± 0.08 [e]	3.08 ± 0.14	0.149 ± 0.027 [f]

[a] k_{RB} was (5.90 ± 0.03) x 10^{-3} min^{-1}; [b] Values obtained in ethanol, with RB as a reference photosensitizer; [c] S_{RB} = (1.15 ± 0.04) x 10^8; [d] Ethanolic solution, Quinine sulfate as a reference and λ_{exc}=330 nm; [e] With perinaphtenone as a reference [47]. [f] Φ_f = 0.16 was reported for the 6-MeOQ ligand [2].

The considerably high results obtained for the Singlet Oxygen and Fluorescence Quantum Yields suggest that these complexes can be used in $^1O_2$-involving applications and in fluorescence related processes.

3.5 Thermogravimetric properties

TGA and DTA experiments were carried out to study the thermal decomposition of the complexes **II** and **V** and are presented in Figure S12 in the ESI. TG and DT studies have already been reported for **I, III** and **IV** [7].

The TG curve of **II** reveals that the decomposition takes place in four steps. The first one is consistent with the evolution of one 6-MeOQ ligand (observed: 33.7% and expected: 35.3%). The other quinoline decomposes in the next two steps (experimental: 34.6 % and expected: 35.3 %). Finally, a weight loss of 11.3 % is consistent with the formation of NiO as a final product (calculated: 12.1 %). The decomposition of the complex takes place with three endothermic peaks as observed in DT curve and the last process could not be observed. For **V** the DT curve shows an endothermic peak at 167 ºC due to the melting point. The first weight loss (64.3 %) occurs immediately after the fusion process and is consistent with the evolution of the two 6-MeOQ ligands (calculated: 65.2 %). Then, the remaining $AgNO_3$ decomposes above 300 ºC to produce Ag(0) as expected [48] (observed loss: 12.5 %; expected: 12.7 %). Both decomposition steps are exothermic as evidenced in the DT curve.

3.6 Antibacterial Activity

The antibacterial activity of the complexes and the 6-MeOQ free ligand has been tested. The results of the assays are summarized in Figure 7. For all the strains, the negative control (DMSO 6%) did not show growth inhibition activity, while the positive control (TEGO 51 ®) has shown the expected inhibitory effect. The free ligand showed a low growth inhibition (diameters of inhibition between 9.7 - 12.0 mm) upon *B. cereus* and *E. coli*. In the former, the effect was observed for both doses, but in the latter, the effect was evidenced only at the highest one. The free ligand had no effect upon the growth of *S. aureus* nor *S. typhimurium*, however upon complexation all the compounds caused an inhibition growth effect ($p < 0.0001$). In all the strains, **I** was the most active, which showed to be statistically more effective than the free ligand at all the tested doses ($p < 0.0001$). In all the strains **II** exerted a higher effect than the 6-MeOQ at both doses ($p < 0.0001$), apart from *B. cereus* where no significative differences were found at the lower dose ($p > 0.05$). A similar behavior was observed for **III,** which showed more activity than the ligand ($p < 0.0001$), excepting *B. cereus* at the highest dose ($p > 0.05$). The observed effect upon *B. cereus* for **IV** and **V** was not statistically different to that of the ligand ($p > 0.05$). However, upon *E. coli*, **IV** was more active than the 6-MeOQ at the lower dose and **V** at both doses ($p < 0.0001$).

View Article Online
DOI: 10.1039/C8NJ00661J

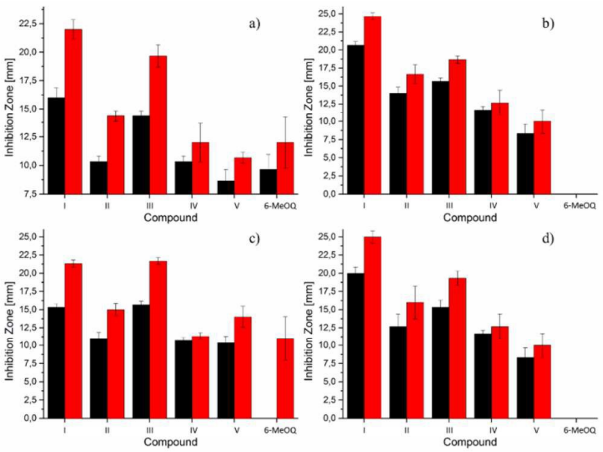

Figure 7. Diameter of the inhibition zones ± SD [mm] for *B. cereus* (a), *S. aureus* (b), *E. coli* (c) and *S. typhimurium* (d) for complexes **I - V** and 6-MeOQ ligand. Black: 400 µg; Red: 600 µg.

Conclusions

In summary, Co(II), Ni(II), Cu(II), Zn(II) and Ag(I) complexes with 6-MeOQ as ligand have been synthesized and their crystal structures have been studied for the first time. Hirshfeld Surface analysis has shown that the crystal lattices of all the complexes are influenced for the presence of several intermolecular interactions, including hydrogen bonds and π ··· π stacking interactions. The spectroscopic data are in good agreement with the crystallographic results. The values obtained for the Singlet Oxygen generation and Fluorescence quantum yields are a good indicator of the possibility for the use of these complexes in photochemical related processes (e.g. advanced oxidation processes and the development of new light emitting devices).

The antimicrobial effect was improved for *S. aureus* and *S. typhimurium* and at least was retained in *B. cereus* and *E. coli* strains after complexation.

Conflicts of interest

There are not conflicts of interest to declare.

Acknowledgements

The authors would like to thank Universidad Nacional de Colombia (Hermes 35753) a COLCIENCIAS from Colombia, and Universidad Nacional de La Plata, CONICET and ANPCyT from Argentina for providing financial support. Finally, thanks to Claudia Núñez for her contribution to the writing of this article.

References

1 K. Kaur, M. Jain, R. P. Reddy and R. Jain, *Eur. J. Med. Chem.*, 2010, **45**, 3245–3264.
2 S. G. Schulman, R. M. Threatte, a C. Capomacchia and W. L. Paul, *J. Pharm. Sci.*, 1974, **63**, 876–80.
3 C. Villa-Pérez, I. C. Ortega, A. M. Payán-Aristizábal, G. Echeverría, G. C. Valencia-Uribe and D. B. Soria, *Zeitschrift für Naturforsch. B*, 2015, **70**, 719–725.
4 T. Ikeyama, T. Azumi, T. Murao and I. Yamazaki, *Chem. Phys. Lett.*, 1983, **96**, 419–421.
5 Y. T. Varma, S. Joshi and D. D. Pant, 2013, vol. 1123, pp. 1123–1124.
6 Y. T. Varma and D. D. Pant, *Spectrochim. Acta - Part A Mol. Biomol. Spectrosc.*, 2016, **158**, 9–17.
7 J. R. Allan and J. Dahyrnple, *Thermochim. Acta*, 1991, **191**, 223–230.
8 C. Villa-Pérez, I. Oyarzabal, G. A. Echeverría, G. C. Valencia-Uribe, J. M. Seco and D. B. Soria, *Eur. J. Inorg. Chem.*, 2016, **2016**, 4835–4841.
9 P. Shinde, S. Pandharipande, N. Thejokalyani and S. J. Dhoble, *Optik (Stuttg).*, 2018, **162**, 151–160.
10 M. Wallesch, M. Nieger, D. Volz and S. Bräse, *Inorg. Chem. Commun.*, 2017, **86**, 232–240.
11 B. Zhang, H. Liu, F. Wu, G. F. Hao, Y. Chen, C. Tan, Y. Tan and Y. Jiang, *Sensors Actuators, B Chem.*, 2017, **243**, 765–774.
12 M. I. Abou-Dobara, M. A. Diab, A. Z. El-Sonbati, A. A. El-Bindary and A. M. Barakat, *Arab. J. Chem.*, 2017, **10**, S1316–S1327.
13 H. F. Abd El-Halim, G. G. Mohamed and M. N. Anwar, *Appl. Organomet. Chem.*, 2018, **32**, 1–12.
14 H. F. Abd El-Halim, M. M. Omar and M. N. Anwar, *J. Therm. Anal. Calorim.*, 2017, **130**, 1069–1083.
15 L. J. Zhang, J. A. Zhang, X. Z. Zou, Y. J. Liu, N. Li, Z. J. Zhang and Y. Li, *Bioorganic Med. Chem. Lett.*, 2015, **25**, 1778–1781.
16 Y.-Y. Zhao, X.-H. Zhao, J. Zhang, J.-G. Pan and X. Li, *Acta Crystallogr. Sect. C Cryst. Struct. Commun.*, 2013, **69**, 1096–1099.
17 X. Z. Zou, J. A. Zhang, L. J. Zhang, Y. J. Liu, N. Li, Y. Li, S. C. Wei and M. Pan, *Inorg. Chem. Commun.*, 2015, **54**, 21–24.
18 A. W. Bauer, W. M. Kirby, J. C. Sherris and M. Turk, *Am. J. Clin. Pathol.*, 1966, **45**, 493–496.
19 F. Rowe, S. Vargas Superti, R. Machado Scheibe and C. G. Dias, *Diagn. Microbiol. Infect. Dis.*, 2002, **43**, 45–48.
20 A. Berahou, A. Auhmani, N. Fdil, A. Benharref, M. Jana and C. A. Gadhi, *J. Ethnopharmacol.*, 2007, **112**, 426–429.
21 F. Wilkinson, W. P. Helman and A. B. Ross, *J. Phys. Chem. Ref. Data*, 1993, **22**, 113.
22 A. T. R. Williams, S. A. Winfield and J. N. Miller, *Analyst*, 1983, **108**, 1067.
23 J. W. Eaton, D. Bateman, S. Hauberg and R. Wehbring, 2017.
24 W. H. Melhuish, *J. Phys. Chem.*, 1961, **65**, 229–235.
25 CrysAlis CCD, 2006.
26 G. M. Sheldrick, *Acta Crystallogr. A.*, 2008, **64**, 112–22.
27 G. M. Sheldrick, SHELXS-97, Program for Crystal Structure Resolution, 1997.
28 G. M. Sheldrick, SHELXL-97, Program for Crystal Structure Analysis, 1997.
29 S. K. Wolff, D. J. Grimwood, J. J. McKinnon, M. J. Turner, D. Jyatilaka and M. A. Spackman, 2012.
30 M. A. Spackman and J. J. McKinnon, *Crystengcomm*, 2002, **4**, 378–392.
31 J. J. McKinnon, M. A. Spackman and A. S. Mitchell, *Acta Crystallogr. Sect. B Struct. Sci.*, 2004, **60**, 627–668.
32 D. J. Carter, P. Raiteri, K. R. Barnard, R. Gielink, M.

View Article Online
DOI: 10.1039/C8NJ00661J

Mocerino, B. W. Skelton, J. G. Vaughan, M. I. Ogden and A. L. Rohl, *CrystEngComm*, 2017, **19**, 2207–2215.
33 T. Williams and C. Kelley and many others, 2017.
34 M. Llunell, D. Casanova, J. Cirera, J. M. Bofill, P. Alemany, S. Alvarez, M. Pinsky and D. Avnir, 2005.
35 H. Schmidbaur and A. Schier, *Angew. Chemie - Int. Ed.*, 2015, **54**, 746–784.
36 Y. Zhou, W. Chen and D. Wang, *Dalt. Trans.*, 2008, 1444.
37 L. Fabbrizzi, M. Licchelli, P. Pallavicini, D. Sacchi and A. Taglietti, *Anal. (Cambridge, U. K.)*, 1996, **121**, 1763–1768.
38 N. J. Turro, *Modern Molecular Photochemistry, p. 191*, University Science Books, U.S, 1st edn., 1991.
39 K. Itoh and T. Azumi, *J. Chem. Phys.*, 1975, **62**, 3431.
40 S. M. Pradeepa, H. S. Bhojya Naik, B. Vinay Kumar, K. Indira Priyadarsini, A. Barik and T. R. Ravikumar Naik, *Spectrochim. Acta - Part A Mol. Biomol. Spectrosc.*, 2013, **101**, 132–139.
41 C. Mari, H. Huang, R. Rubbiani, M. Schulze, F. Würthner, H. Chao and G. Gasser, *Eur. J. Inorg. Chem.*, 2017, **2017**, 1745–1752.
42 A. W. Varnes, R. B. Dodson and E. L. Wehry, *J. Am. Chem. Soc.*, 1972, **94**, 946–950.
43 J. A. Kemlo and T. M. Shepherd, *Chem. Phys. Lett.*, 1977, **47**, 158–162.
44 P. G. Cozzi, L. S. Dolci, A. Garelli, M. Montalti, L. Prodi and N. Zaccheroni, *New J. Chem.*, 2003, **27**, 692–697.
45 A. Majumder, G. M. Rosair, A. Mallick, N. Chattopadhyay and S. Mitra, *Polyhedron*, 2006, **25**, 1753–1762.
46 C. J. P. Monteiro, M. M. Pereira, M. E. Azenha, H. D. Burrows, C. Serpa, L. G. Arnaut, M. J. Tapia, M. Sarakha and P. Wong-wah-chung, *Photochem. Photobiol. Sci*, 2005, **4**, 617–624.
47 C. Valencia, Universidad de Chile, (PhD Thesis), 2003.
48 K. Otto, I. Oja Acik, M. Krunks, K. Tõnsuaadu and A. Mere, *J. Therm. Anal. Calorim.*, 2014, **118**, 1065–1072.

View Article Online
DOI: 10.1039/C8NJ00661J

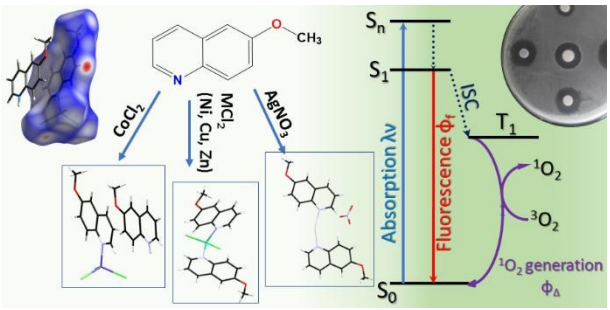

Five complexes with 6-Methoxyquinoline have been synthesized; their structural, spectroscopic, photophysical and biological properties have been studied.